Sodium-Ion Batteries Hot Paper

Deutsche Ausgabe: DOI: 10.1002/ange.201802672
Internationale Ausgabe: DOI: 10.1002/anie.201802672

Robust SnO_{2-x} Nanoparticle-Impregnated Carbon Nanofibers with Outstanding Electrochemical Performance for Advanced Sodium-Ion Batteries

Dingtao Ma[+], Yongliang Li[+], Hongwei Mi, Shan Luo, Peixin Zhang, Zhiqun Lin,* Jianqing Li, and Han Zhang*

Abstract: *The sluggish sodium reaction kinetics, unstable Sn/Na_2O interface, and large volume expansion are major obstacles that impede practical applications of SnO_2-based electrodes for sodium-ion batteries (SIBs). Herein, we report the crafting of homogeneously confined oxygen-vacancy-containing SnO_{2-x} nanoparticles with well-defined void space in porous carbon nanofibers (denoted SnO_{2-x}/C composites) that address the issues noted above for advanced SIBs. Notably, SnO_{2-x}/C composites can be readily exploited as the working electrode, without need for binders and conductive additives. In contrast to past work, SnO_{2-x}/C composites-based SIBs show remarkable electrochemical performance, offering high reversible capacity, ultralong cyclic stability, and excellent rate capability. A discharge capacity of 565 mAh g^{-1} at 1 A g^{-1} is retained after 2000 cycles.*

The past few decades have witnessed substantial advances in the utilization of low-cost, renewable energy sources to meet the global demand. Sodium-ion batteries (SIBs) have developed rapidly as they have attractive attributes, such as decent energy density, excellent sustainability, and abundant, low-cost sodium resources.[1,2] The electrode materials with high discharge capacity, outstanding rate capability, and long cycle life are the key to high performance SIBs.[3,4] Recently, SnO_2 has garnered much attention because of its high abundance, large theoretical capacity and nontoxicity. However, the large volume expansion and low intrinsic conductivity greatly plague its practical applications.[5,6] The reactions between SnO_2 and Na can be described as follows [Eqs. (1)–(3)]:

$$SnO_2 + 2\,Na^+ + 2\,e^- \rightarrow SnO + Na_2O \quad (1)$$

$$SnO + 2\,Na^+ + 2\,e^- \rightarrow Sn + Na_2O \quad (2)$$

$$Sn + x\,Na^+ + x\,e^- \leftrightarrow Na_xSn\ (0 \le x \le 3.75) \quad (3)$$

The SnO_2 conversion [i.e., Eq. (1) and (2)] offers a theoretical capacity of 710 mAh g^{-1}. However, such irreversible conversion usually leads to a fast capacity fading after the initial cycle.[7,8] In contrast, Sn can be reversibly alloyed [i.e., Eq. (3)] with up to 3.75 mol of Na^+, resulting in a theoretical capacity of 665 mAh g^{-1}, while accompanying by a large volume expansion of over 400% and the aggregation of metallic Sn upon cycling. The latter in turn causes the mechanical failure and the formation of unstable solid electrolyte interface (SEI) film. It is also notable that the low conductivity of SnO_2 leads to poor reaction kinetics and rate capability.[9]

The enhanced electrochemical performance can usually be achieved by nanosizing SnO_2 and binding with the conductive matrix.[10–12] However, despite these strategies that can effectively suppress the volume expansion and accelerate the ionic and electronic transportation to some extent, they cannot retain the long-term stability and rate capability. This is because the nanostructured SnO_2 would inevitably tend to crack, detach from the conductive matrix and diminish the electronic contact during electrochemical reactions.[13,14] The use of defects, such as oxygen vacancies, has been proved to effectively dominate the electronic structure of semiconductor oxides for a wide range of applications, such as to improve the cyclability and rate capability for batteries.[15,16]

In this context, we report a robust strategy for crafting oxygen-vacancy-containing SnO_{2-x} nanoparticle-encapsulated carbon nanofibers with outstanding electrochemical performance for advanced SIBs. Intriguingly, flexible and free-standing "mats" composed of SnO_{2-x}/C composites can be directly employed as electrodes in SIBs, eliminating the addition of binders and conductive additives, thus not only markedly increasing energy density but also showing great potential for flexible energy storage devices.[17,18] The SnO_{2-x}/C composite-based SIBs display an array of out-

[*] D. Ma,[+] Dr. Y. Li,[+] Dr. H. Mi, S. Luo, Prof. P. Zhang
College of Chemistry and Environmental Engineering
Shenzhen University
Shenzhen, 518060 (China)
E-mail: pxzhang@szu.edu.cn
Prof. Z. Lin
School of Materials Science and Engineering
Georgia Institute of Technology
Atlanta, GA 30332 (USA)
E-mail: zhiqun.lin@mse.gatech.edu
D. Ma,[+] Prof. J. Li
Faculty of Information Technology
Macau University of Science and Technology
Macau, 519020 (China)
D. Ma,[+] Prof. H. Zhang
SZU-NUS Collaborative Innovation Center for Optoelectronic Science and Technology and Key Laboratory of Optoelectronic Devices and Systems of Ministry of Education and Guangdong Province,
Shenzhen University
Shenzhen, 518060 (China)
[+] These authors contributed equally to this work.
Supporting information and the ORCID identification number(s) for the author(s) of this article can be found under: https://doi.org/10.1002/anie.201802672.

standing electrochemical performance, including high reversible capacity, ultralong cyclic stability, and excellent rate capability. The discharge capacities of SIBs of 634 mAh g^{-1} at 0.1 A g^{-1}, 602 mAh g^{-1} at 0.2 A g^{-1}, 565 mAh g^{-1} at 1 A g^{-1} and 447 mAh g^{-1} at 2 A g^{-1} were found to retain after 300, 800, 2000, and 2500 cycles, respectively. This effective strategy opens up new possible routes for addressing the fundamental challenges of fabricating high-performance SnO_2-based SIBs.

Figure 1 a illustrates the route to the SnO_{2-x}/C electrode based on a flowable sulfur template and electrospinning technique (see Supporting Information for detailed experimental description). It is important to note that oxygen vacancies were found to emerge on the surface of SnO_2 nanocrystals (i.e., changing from SnO_2 to SnO_{2-x}; Figures S1, S2 and S3 in the Supporting Information) as revealed by the XRD and XPS studies discussed below. Figure 1 b shows that the freestanding SnO_{2-x}/C electrode was composed of highly uniform nanofibers with an average diameter of approximately 500 nm. A close-up of Figure S4 reveals that there are many macroporous holes along the SnO_{2-x}/C nanofibers (Figure 1 c). Such relatively large holes allow for the easy penetration of electrolyte and fast transportation of Na^+ ions. Moreover, no obvious SnO_{2-x} nanoparticles were observed on the surface of nanofibers, indicating the full encapsulation of SnO_{2-x} nanoparticles within carbon nanofibers. Transmission electron microscopy (TEM) study was performed to examine the inner structure of SnO_{2-x}/C nanofibers. Figure 1 c,d clearly demonstrate that SnO_{2-x} nanoparticles were highly dispersed within carbon nanofibers with appropriate void space, which is beneficial for alleviating the volume expansion and pulverization. Moreover, the one-dimensional carbon matrix also imparts the fast electronic transfer, thereby improving the electrochemical properties.[19,20] High-resolution TEM image reveals that SnO_{2-x} nanoparticles possess good crystallinity, and a lattice spacing of 0.33 nm can be ascribed to the (110) plane (inset in Figure 1 e). The corresponding energy dispersive X-ray spectroscopy (EDS) analysis (Figure S6) also demonstrates the uniform elemental distribution of C, N, Sn, and O in SnO_{2-x}/C composites. The as-fabricated flake-type SIB was assembled to power commercial LEDs (Figure S7). It is notable that these red LEDs can be readily lit, even when the SIB was bent to 90°, 180° or twisted, signifying the great potential for flexible devices.

Figure 2 a shows the X-ray diffraction (XRD) patterns for SnO_{2-x}/C and SnO_2. The major diffraction peaks of both samples can be indexed as rutile-phase SnO_2. Interestingly, further scrutiny of (110), (101), and (200) peak positions reveals the shift to a lower angle associated with the formation of oxygen vacancies.[16,21] Thermogravimetric analysis (TGA) shows that the mass content of SnO_{2-x} nanoparticles in SnO_{2-x}/C composites is approximately 54 % (Figure S8). X-ray photoelectron spectroscopy (XPS) measurements were carried out to reveal the redox states of Sn, O, and N elements. Two peaks located at the binding energies of 495.5 and 487 eV can be assigned to Sn 3d3/2 and Sn 3d5/2 for SnO_2, respectively (Figure 2 b). Notably, a blue-shift of approximately 0.3 eV in the SnO_{2-x}/C electrode relative to that of SnO_2 noted above was seen. Together with the XRD study, this observation signifies the formation of oxygen vacancies.[6,16,22] In sharp contrast to the SnO_2 sample, the full XPS spectrum of the SnO_{2-x}/C electrode clearly demonstrates the presence of N element (Figure S10a). The deconvolution of N signals yields three main peaks distributed at 398.2, 400.1, and 400.9 eV, which can be ascribed to pyridinic-,

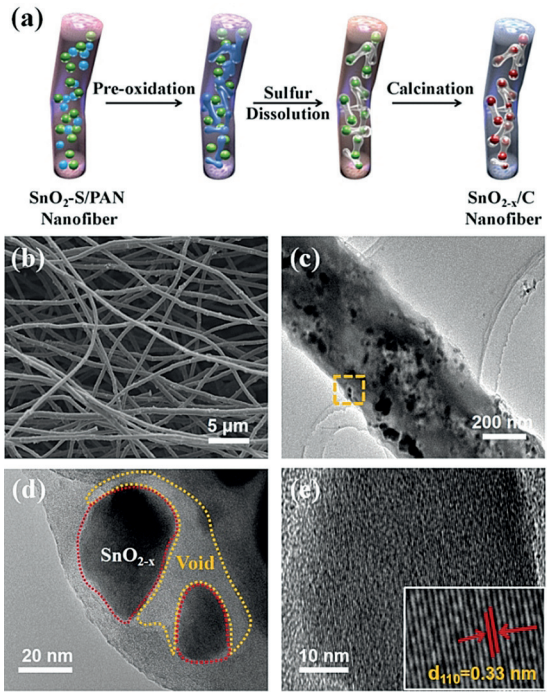

Figure 1. a) Schematic illustration of the formation of SnO_{2-x}/C nanofibers. b) FESEM images. c)–e) TEM and HRTEM images of SnO_{2-x}/C electrode. d) is the close-up of the dashed-box region in (c), and e) is the close-up of the central region in (d); inset shows the (100) plane of the SnO_{2-x} nanoparticles.

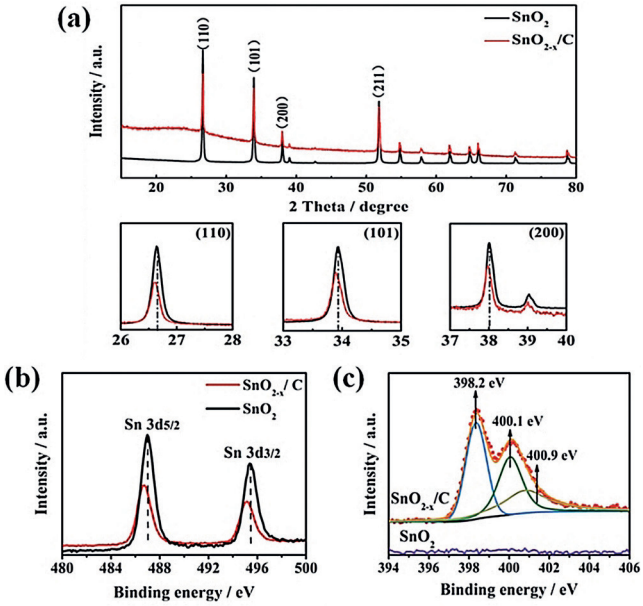

Figure 2. a) X-ray diffraction (XRD) patterns of SnO_2 and SnO_{2-x}/C electrodes. The lower three panels are the close-ups of the (110), (101), and (200) peaks. b),c) XPS spectra of SnO_2 and SnO_{2-x}/C electrodes: b) Sn 3d, and c) N 1s.

pyrrolic-, and quaternary-N, respectively (Figure 2c), and thus may improve the electronic conductivity of the SnO_{2-x}/C electrode.[23–25]

Figure 3a shows the cycling performance of SnO_{2-x}/C and SnO_2 electrodes at 0.1 A g^{-1}. The discharge capacity of the first two cycles were 1185 and 654 mAh g^{-1} for SnO_{2-x}/C, and 1277 and 565 mAh g^{-1} for SnO_2, corresponding to the initial capacity retention (ICE) of 55.2% and 44%, respectively. As the cycling continued, the capacity of pristine SnO_2 gradually decayed and reached 60 mAh g^{-1} after the 195th cycle. In stark contrast, the SnO_{2-x}/C electrode displays an outstanding stability with a discharge capacity of 634 mAh g^{-1} after 300 cycles. Figure 3b compares the rate capability of SnO_{2-x}/C and SnO_2 electrodes at the current densities of 0.1, 0.5, 1, 2, and 5 A g^{-1}. Clearly, SnO_{2-x}/C displays the better high rate performance with higher specific capacity, varying from 646 to 608, 548, 440, and 340 mAh g^{-1} at 0.1, 0.5, 1, 2, and 5 A g^{-1}, respectively. Remarkably, when the current rate turned back to 0.1 A g^{-1} after 50 cycles, the reversible capacity can recover 630 mAh g^{-1}. The capacity retention is 52.6% for SnO_{2-x}/C, which is more than 5-fold higher than that for pristine SnO_2 (i.e., 9.3%) when the discharge rate increases from 0.1 to 5 A g^{-1}. Galvanostatic charge/discharge curves of SnO_{2-x}/C at different current densities are depicted in Figure S11, where all profiles show the distinct features, suggesting the similar reaction processes.

Cyclic voltammetry (CV) measurements were conducted to scrutinize the Na^+ storage behavior of SnO_{2-x}/C and SnO_2. Figure 3c,d display the first three CV profiles of SnO_{2-x}/C and SnO_2 electrodes at a scan rate of 0.1 mV s^{-1}, respectively. Compared with SnO_{2-x}/C electrode, a broad peak in the range of 0.75–1.3 V of SnO_2 electrode in the initial discharge process was observed, which can be attributed to the conversion reactions of $SnO_2 \rightarrow SnO \rightarrow Sn$ [Eq. (1) and (2)], as well as the irreversible formation of the SEI film caused by the electrolyte decomposition on the surface of active materials. Moreover, the peak located in the range of 0.01–0.6 V for both SnO_2 and SnO_{2-x}/C electrodes can be ascribed to the reversible alloying reaction of $Sn \leftrightarrow Na_xSn$ [Eq. (3)]. On the basis of the comparison of charging/discharging analysis of SnO_{2-x}/C and SnO_2 electrodes shown in Figure S12, it is clear that the SEI formation is more stable and the irreversible loss is much less for the SnO_{2-x}/C electrode. In the following anodic scan, the obvious peaks at 0.5, 1.05, and 1.25 V of SnO_{2-x}/C electrode can be ascribed to the dealloying of Na_xSn to Sn, the oxidation of Sn to SnO, and the further oxidation of SnO to SnO_2, respectively. In sharp contrast, only a peak at 0.45 V and a weak peak at 0.65 V can be observed for the SnO_2 electrode, indicating the highly reversible Na^+ reaction kinetic of SnO_{2-x}/C electrode. Moreover, the CV curves of SnO_{2-x}/C and SnO_2 electrodes at various scan rates from 0.1 to 0.7 mV s^{-1} are also shown in Figure S13a and S13b, respectively. It can be seen that the pristine SnO_2 sample exhibits an obvious polarization with the increasing scan rate (marked with an arrow, Figure S13b), while the SnO_{2-x}/C electrode continue displaying the similar reaction kinetic even at higher working current (Figure S13a), demonstrating an outstanding rate capability.

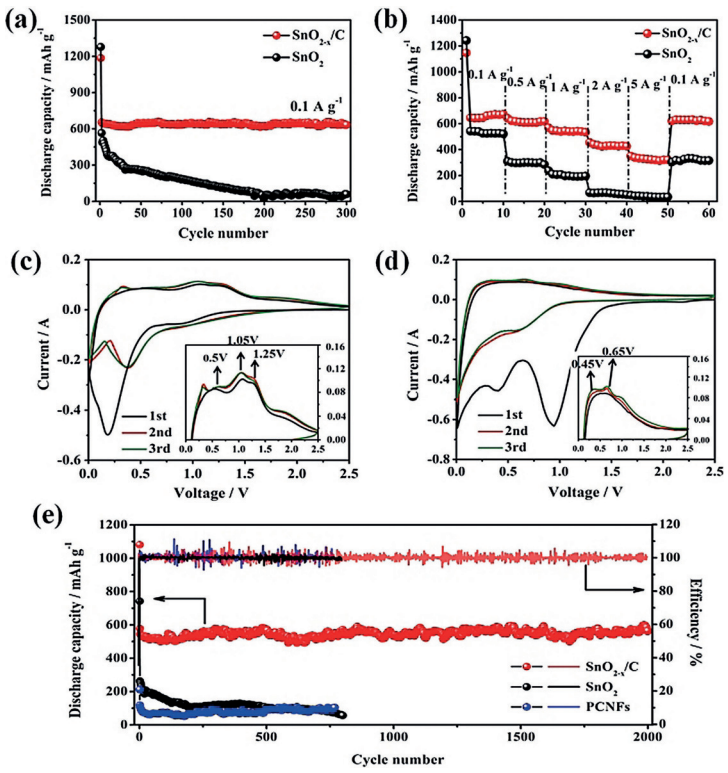

Figure 3. a) Cycling performance of SnO_2 and SnO_{2-x}/C electrodes at 0.1 A g^{-1}. b) Rate capability of SnO_2 and SnO_{2-x}/C electrodes. c), d) CV curves of c) SnO_{2-x}/C and d) SnO_2 electrodes for the first three cycles. e) Cycling performance of SnO_{2-x}/C, SnO_2, and porous carbon nanofibers (PCNFs) electrodes at 1 A g^{-1}, demonstrating long cycling stability of SnO_{2-x}/C electrode (2000 cycles) at high current density.

Figure 3e shows the long-term cycling test for SnO_{2-x}/C, SnO_2 and pure porous carbon nanofibers (PCNFs) electrodes at 1 A g^{-1} with the initial discharge capacities of 1080, 742, and 211 mAh g^{-1} (corresponding to the ICEs of 53.5, 35.5, and 56%), respectively. A discharge capacity of 565 mAh g^{-1} was retained for the SnO_{2-x}/C electrode after 2000 cycles, which contrasts sharply to only 57 mAh g^{-1} after 800 cycles for the pristine SnO_2 electrode. Moreover, importantly, the SnO_{2-x}/C electrode also achieved and maintained 602 and 447 mAh g^{-1} after 800 and 2500 cycles with the Coulombic efficiencies of 97.6% and 106% at the current densities of 0.2 and 2 A g^{-1}, respectively (Figure S14), which may be attributed to the synergy of the unique nanostructure and the gradual activation of active materials. It is worth noting that these are the best high-rate and high-cyclic-stability results of SIBs compared to those reported in literature (Table S1). Figure 4a summarizes the XRD patterns of SnO_{2-x}/C electrode at various voltages after the 20th cycle. Clearly, there exist three main characteristic peaks, that is, 110, 101, and 211 at 2θ of 26.6°, 33.9°, and 51.8°, respectively, for the fresh electrode. As the discharge (i.e., sodiation) process advances, the peak intensities corresponding to SnO_{2-x}/C composite decrease,

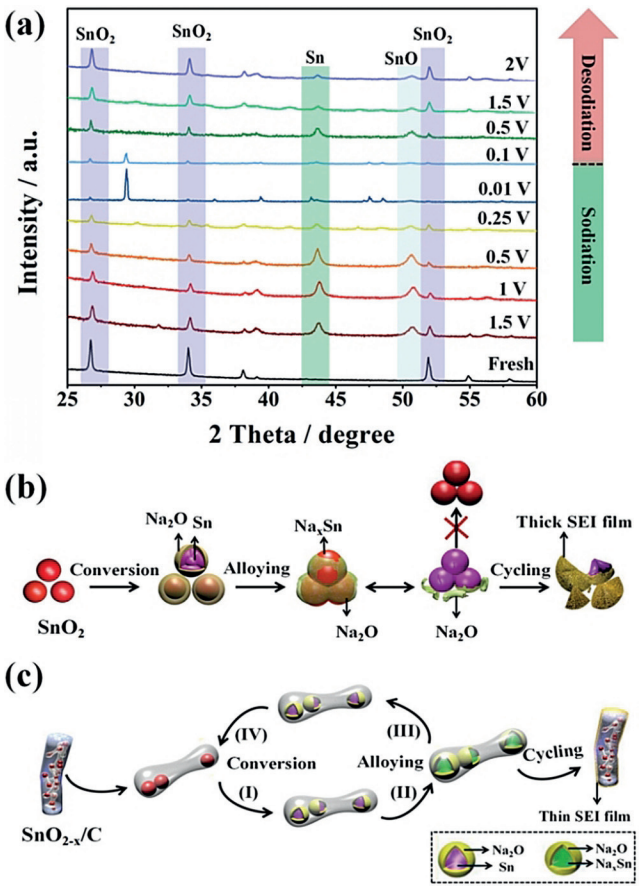

Figure 4. a) Ex-situ XRD patterns of SnO_{2-x}/C electrode after the 20th cycle at 0.05 A g^{-1} between 0.01 and 2.5 V. b), c) The proposed reaction mechanisms of: b) SnO_2 and c) SnO_{2-x}/C electrodes during the charge/discharge process.

accompanied by the emergence of new peaks at 2θ of 50.7° and 43.8° ascribed to SnO and Sn phases, signifying the progressive conversion of SnO_2 (i.e., $SnO_2 \rightarrow SnO \rightarrow Sn$). Quite intriguingly, all the peaks belonging to SnO_2, SnO and Sn tend to disappear when discharged to 0.01 V, and the peaks at 2θ of 29.4°, 47.5° and 48.6° may be attributed to Na_xSn alloy phases, manifesting the full alloying reaction between Sn and Na^+. Conversely, as the desodiation process continues, the peaks of Na_xSn alloyed phase gradually disappear, associated with the recovery of Sn, SnO, and SnO_2 phases.

On the basis of all the results described above, we conceived the reaction mechanisms of SnO_2 and SnO_{2-x}/C electrode during the charge/discharge process as illustrated in Figure 4b,c. Typically, for the SnO_2 electrode, the generated metallic Sn nanoparticles and amorphous Na_2O tend to separate and self-aggregate[26] (second panel in Figure 4b). Moreover, the next alloying reaction [Eq. (3)] further promotes the separation of Na_2O from the Na_xSn/Na_2O interface due to the volumetric strain (third panel in Figure 4b), thus hindering the conversion of $Sn \rightarrow SnO_2$. Furthermore, Sn nanoparticles tend to aggregate, pulverization, and finally form cracks during the cycling process (Figure S19), which is primarily caused by the large volumetric stress and eventually leads to severe capacity fading in the following cycles. In stark contrast, in the present study, the rationally designed SnO_{2-x}/C electrodes resolved these issues and greatly improved the energy storage performance. First, the convenient yet robust homogeneous confinement of SnO_{2-x} nanoparticles within microporous carbon nanofibers not only greatly prevents the separation and aggregation of Sn and Na_2O phases (second to fourth panels in Figure 4c) that occur in pristine SnO_2 electrode case discussed above, but also effectively suppresses the large volume variation during the charge/discharge process (Figure 4c). Second, the one-dimensional porous carbon matrix of SnO_{2-x}/C electrode provides the effective pathway for facilitating the charge transfer and ionic insertion, and moreover functions as artificial barrier to form stable SEI film[27] (fifth panel in Figure 4c), as clearly evident in the insets of Figure S17b, S17d and S17f. Third, the presence of oxygen vacancies within SnO_{2-x} nanoparticles imparts the lowering of the reaction energy barrier and the enhancement of the intrinsic electronic conductivity.

In summary, we developed a viable strategy by crafting oxygen-vacancy-containing SnO_{2-x} nanoparticle-impregnated carbon nanofibers (i.e., SnO_{2-x}/C composites) as electrodes for advanced SIBs with outstanding electrochemical performance (i.e., high reversible capacity, long cyclic stability, and excellent rate capability). Such intriguing nanoparticle-encapsulated one-dimensional conductive nanofiber architectures not only retain the intrinsic advantages of nanosizing SnO_{2-x}, but also offer benefits, such as effectively restraining the volume variation and enhancing the SnO_2 conversion kinetics [Eqs. (1) and (2)]. Consequently, the SnO_{2-x}/C composite exhibits remarkable reversibility of the $Sn \rightarrow SnO_2$ conversion and high specific capacity with excellent cyclic stability. As such, the strategy developed herein may open up opportunities to produce other metal-oxide-nanoparticle-containing carbon fibers as electrodes for high-performance energy-storage systems including sodium-/lithium-ion batteries.

Acknowledgements

This work is supported by the National Natural Science Foundation of China (No. 51774203) and the Foundation of Guangdong Educational Committee (No. 2016KTSCX124), Shenzhen Science and Technology Project Program (Nos. JCYJ20160422112012739, KQJSCX20170327151152722).

Conflict of interest

The authors declare no conflict of interest.

Keywords: carbon nanofibers · energy storage · SnO_2 nanoparticles · sodium-ion batteries

How to cite: *Angew. Chem. Int. Ed.* **2018**, *57*, 8901–8905
Angew. Chem. **2018**, *130*, 9039–9043

[1] J. Y. Hwang, S. T. Myung, Y. K. Sun, *Chem. Soc. Rev.* **2017**, *46*, 3529–3614.

[2] H. Tavassol, E. M. Jones, N. R. Sottos, A. A. Gewirth, *Nat. Mater.* **2016**, *15*, 1182 – 1187.
[3] D. Kundu, E. Talaie, V. Duffort, L. F. Nazar, *Angew. Chem. Int. Ed.* **2015**, *54*, 3431 – 3448; *Angew. Chem.* **2015**, *127*, 3495 – 3513.
[4] B. Jiang, C. Han, B. Li, Y. He, Z. Lin, *ACS Nano* **2016**, *10*, 2728 – 2735.
[5] J. Liang, X. Y. Yu, H. Zhou, H. B. Wu, S. Ding, X. W. Lou, *Angew. Chem. Int. Ed.* **2014**, *53*, 12803 – 12807; *Angew. Chem.* **2014**, *126*, 13017 – 13021.
[6] L. P. Wang, Y. Leconte, Z. Feng, C. Wei, Y. Zhao, Q. Ma, W. Xu, S. Bourrioux, P. Azais, M. Srinivasan, Z. J. Xu, *Adv. Mater.* **2017**, *29*, 1603286.
[7] R. Hu, D. Chen, G. Waller, Y. Ouyang, Y. Chen, B. Zhao, B. Rainwater, C. Yang, M. Zhu, M. Liu, *Energy Environ. Sci.* **2016**, *9*, 595 – 603.
[8] B. Jiang, Y. He, B. Li, S. Zhao, S. Wang, Y. B. He, Z. Q. Lin, *Angew. Chem. Int. Ed.* **2017**, *56*, 1869 – 1872; *Angew. Chem.* **2017**, *129*, 1895 – 1898.
[9] S. Y. Lee, K. Y. Park, W. S. Kim, S. Yoon, S. H. Hong, K. Kang, M. Kim, *Nano Energy* **2016**, *19*, 234 – 245.
[10] S. Wu, R. Xu, M. Lu, R. Ge, J. Iocozzia, C. Han, B. Jiang, Z. Lin, *Adv. Energy Mater.* **2015**, *5*, 1500400.
[11] X. Zhou, L. Yu, X. W. Lou, *Adv. Energy Mater.* **2016**, *6*, 1600451.
[12] S. Zhao, Z. Wang, Y. He, B. Jiang, Y. Harn, X. Liu, F. Yu, F. Feng, Q. Shen, Z. Lin, *ACS Energy Lett.* **2017**, *2*, 111 – 116.
[13] R. Hu, Y. Ouyang, T. Liang, H. Wang, J. Liu, J. Chen, C. Yang, L. Yang, M. Zhu, *Adv. Mater.* **2017**, *29*, 1605006.
[14] T. Sun, Z. J. Li, H. G. Wang, D. Bao, F. L. Meng, X. B. Zhang, *Angew. Chem. Int. Ed.* **2016**, *55*, 10662 – 10666; *Angew. Chem.* **2016**, *128*, 10820 – 10824.
[15] Y. Jiang, S. Yu, B. Wang, Y. Li, W. Sun, Y. Lu, M. Yan, B. Song, S. Dou, *Adv. Funct. Mater.* **2016**, *26*, 5315 – 5321.
[16] H. S. Kim, J. B. Cook, H. Lin, J. S. Ko, S. H. Tolbert, V. Ozolins, B. Dunn, *Nat. Mater.* **2017**, *16*, 454 – 460.
[17] Y. Xu, M. Zhou, X. Wang, C. Wang, L. Liang, F. Grote, M. Wu, Y. Mi, Y. Lei, *Angew. Chem. Int. Ed.* **2015**, *54*, 8768 – 8771; *Angew. Chem.* **2015**, *127*, 8892 – 8895.
[18] X. Dong, L. Chen, X. Su, Y. Wang, Y. Xia, *Angew. Chem. Int. Ed.* **2016**, *55*, 7474 – 7477; *Angew. Chem.* **2016**, *128*, 7600 – 7603.
[19] Y. Zhang, Y. Zhao, J. Ren, W. Weng, H. Peng, *Adv. Mater.* **2016**, *28*, 4524 – 4531.
[20] H. Yin, Q. Li, M. Cao, W. Zhang, H. Zhao, C. Li, K. Huo, M. Zhu, *Nano Res.* **2017**, https://doi.org/10.1007/s12274-016 – 1408-z.
[21] Y. Yao, L. Zeng, S. Hu, Y. Jiang, B. Yuan, Y. Yu, *Small* **2017**, *13*, 1603513.
[22] A. Angelo, N. Webster, A. Chaffee, *Inorg. Chem.* **2016**, *55*, 12595 – 12602.
[23] L. Fan, X. Li, B. Yan, J. Feng, D. Xiong, D. Li, L. Gu, Y. Wen, S. Lawes, X. Sun, *Adv. Energy Mater.* **2016**, *6*, 1502057.
[24] D. Ma, Y. Li, J. Yang, H. Mi, S. Lou, L. Deng, C. Yan, P. Zhang, Z. Lin, X. Ren, J. Li, H. Zhang, *Nano Energy* **2018**, *43*, 317 – 325.
[25] D. Ma, Y. Li, J. Yang, H. Mi, S. Luo, L. Deng, C. Yan, M. Rauf, P. Zhang, X. Sun, X. Ren, J. Li, H. Zhang, *Adv. Funct. Mater.* **2018**, *28*, 1705537.
[26] W. Dong, J. Xu, C. Wang, Y. Lu, X. Liu, X. Wang, X. Yuan, Z. Wang, T. Lin, M. Sui, I. Chen, F. Huang, *Adv. Mater.* **2017**, *29*, 1700136.
[27] L. Zu, Q. Su, F. Zhu, B. Chen, H. Lu, C. Peng, T. He, G. Du, P. He, K. Chen, S. Yang, J. Yang, H. Peng, *Adv. Mater.* **2017**, *29*, 1701494.

Manuscript received: March 3, 2018
Accepted manuscript online: April 23, 2018
Version of record online: May 8, 2018

